Science AAAS

Computational Design of Proteins Targeting the Conserved Stem Region of Influenza Hemagglutinin

Sarel J. Fleishman, *et al.*

Science **332**, 816 (2011);
DOI: 10.1126/science.1202617

This copy is for your personal, non-commercial use only.

If you wish to distribute this article to others, you can order high-quality copies for your colleagues, clients, or customers by clicking here.

Permission to republish or repurpose articles or portions of articles can be obtained by following the guidelines here.

The following resources related to this article are available online at www.sciencemag.org (this infomation is current as of May 18, 2011):

Updated information and services, including high-resolution figures, can be found in the online version of this article at:
http://www.sciencemag.org/content/332/6031/816.full.html

Supporting Online Material can be found at:
http://www.sciencemag.org/content/suppl/2011/05/12/332.6031.816.DC2.html
http://www.sciencemag.org/content/suppl/2011/05/11/332.6031.816.DC1.html

A list of selected additional articles on the Science Web sites **related to this article** can be found at:
http://www.sciencemag.org/content/332/6031/816.full.html#related

This article **cites 19 articles**, 7 of which can be accessed free:
http://www.sciencemag.org/content/332/6031/816.full.html#ref-list-1

This article has been **cited by** 1 articles hosted by HighWire Press; see:
http://www.sciencemag.org/content/332/6031/816.full.html#related-urls

This article appears in the following **subject collections:**
Biochemistry
http://www.sciencemag.org/cgi/collection/biochem

Science (print ISSN 0036-8075; online ISSN 1095-9203) is published weekly, except the last week in December, by the American Association for the Advancement of Science, 1200 New York Avenue NW, Washington, DC 20005. Copyright 2011 by the American Association for the Advancement of Science; all rights reserved. The title *Science* is a registered trademark of AAAS.

30. D. Wenemoser, P. W. Reddien, *Dev. Biol.* **344**, 979 (2010).
31. J. Baguñà, *J. Exp. Zool.* **195**, 53 (1976).
32. M. L. Scimone, J. Meisel, P. W. Reddien, *Development* **137**, 1231 (2010).
33. B. J. Pearson, A. Sánchez Alvarado, *Development* **137**, 213 (2010).
34. K. Nishimura, Y. Kitamura, T. Taniguchi, K. Agata, *Neuroscience* **168**, 18 (2010).
35. E. E. Morrisey *et al.*, *Genes Dev.* **12**, 3579 (1998).
36. C. R. Bardeen, F. H. Baetjer, *J. Exp. Zool.* **1**, 191 (1904).
37. F. Dubois, *Bull. Biol. Fr. Belg.* **83**, 213 (1949).
38. T. Lender, A. Gabriel, *C. R. Acad. Sc. Paris* **260**, 4095 (1965).
39. T. Hayashi, M. Asami, S. Higuchi, N. Shibata, K. Agata, *Dev. Growth Differ.* **48**, 371 (2006).

Acknowledgments: We thank D. Kim for manuscript comments; S. Lapan for neuronal and intestinal markers; M. Srivastava for phylogenetics advice; D. Wenemoser for SMEDWI-1 antibody purification; J. Owen for Illumina data; M. Griffin for flow cytometry assistance; and P. Hsu, G. Bell, R. Young, and all members of the Reddien Lab for extensive comments and discussion. P.W.R. is an early career scientist of the Howard Hughes Medical Institute and an associate member of the Broad Institute of Harvard and MIT. We acknowledge support from the NIH (grant R01GM080639) and the Keck Foundation.

Supporting Online Material
www.sciencemag.org/cgi/content/full/332/6031/811/DC1
Materials and Methods
Figs. S1 to S19
Table S1
References

8 February 2011; accepted 11 April 2011
10.1126/science.1203983

Computational Design of Proteins Targeting the Conserved Stem Region of Influenza Hemagglutinin

Sarel J. Fleishman,[1]* Timothy A. Whitehead,[1]* Damian C. Ekiert,[2]* Cyrille Dreyfus,[2] Jacob E. Corn,[1]† Eva-Maria Strauch,[1] Ian A. Wilson,[2] David Baker[1,3]‡

We describe a general computational method for designing proteins that bind a surface patch of interest on a target macromolecule. Favorable interactions between disembodied amino acid residues and the target surface are identified and used to anchor de novo designed interfaces. The method was used to design proteins that bind a conserved surface patch on the stem of the influenza hemagglutinin (HA) from the 1918 H1N1 pandemic virus. After affinity maturation, two of the designed proteins, HB36 and HB80, bind H1 and H5 HAs with low nanomolar affinity. Further, HB80 inhibits the HA fusogenic conformational changes induced at low pH. The crystal structure of HB36 in complex with 1918/H1 HA revealed that the actual binding interface is nearly identical to that in the computational design model. Such designed binding proteins may be useful for both diagnostics and therapeutics.

Molecular recognition is central to biology, and high-affinity binding proteins, such as antibodies, are invaluable for both diagnostics and therapeutics (*1*). Current methods for producing antibodies and other proteins that bind a protein of interest involve screening large numbers of variants generated by the immune system or by library construction (*2*). The computer-based design of high-affinity binding proteins is a fundamental test of current understanding of the physical-chemical basis of molecular recognition and, if successful, would be a powerful complement to current library-based screening methods, because it would allow targeting of specific patches on a protein surface. Recent advances in computational design of protein interactions have yielded switches in interaction specificity (*3*), methods to generate modest-affinity complexes (*4*, *5*), two-sided design of a novel protein interface (*6*), and design of a high-affinity interaction by grafting known key residues onto an unrelated protein scaffold (*7*). However, the capability to target an arbitrarily selected protein surface has remained elusive.

Influenza presents a serious public health challenge, and new therapies are needed to combat viruses that are resistant to existing antiviral medicines (*8*) or that escape neutralization by the immune system. Hemagglutinin (HA) is a prime candidate for drug development as it is the major player in viral invasion of cells lining the respiratory tract. Although most antibodies bind to the rapidly varying head region of HA, recently two antibodies, CR6261 and F10, were structurally characterized (*9*, *10*) and found to bind to a region on the HA stem, which is conserved among all group 1 influenza strains (fig. S1) (*11*). Here, we describe a computational method for designing protein-protein interactions de novo and use the method to design high-affinity binders to the conserved stem region on influenza HA.

Computational Design Method

In devising the computational design strategy, we considered features common to dissociable protein complexes. During protein complex formation, proteins bury on average ~1600 Å^2 of solvent-exposed surface area (*12*). Interfaces typically contain several residues that make highly optimized van der Waals, hydrogen bonding, and electrostatic interactions with the partner protein; these interaction hot spots contribute a large fraction of the binding energy (*13*).

Our strategy thus centers on the design of interfaces that have both high shape complementarity and a core region of highly optimized, hot spot–like residue interactions (*14*). We engineered high-affinity interactions and high shape complementarity into scaffold proteins in two steps (see Fig. 1): (i) disembodied amino acid residues were computationally docked or positioned against the target surface to identify energetically favorable configurations with the target surface; and (ii) shape-complementary configurations of scaffold proteins were computed that anchor these energetically favorable interactions.

Design of HA-Binding Proteins

The surface on the stem of HA recognized by neutralizing antibodies consists of a hydrophobic groove that is flanked by two loops that place severe steric constraints on binding to the epitope (Fig. 2, A and B) (*15*). In the first step of our design protocol (Fig. 1), the disembodied hot spot residues found through computational docking cluster into three regions contacting HA (HS1, HS2, and HS3) (Fig. 1). In HS1, a Phe side chain forms an energetically favorable aromatic stacking interaction with Trp^{21} on chain 2 of the HA (HA2) (HA residue numbering corresponds to the H3 subtype sequence-numbering convention) (*16*). In HS2, the nonpolar residues Ile, Leu, Met, Phe, and Val, make favorable van der Waals interactions with both the hydrophobic groove and HS1 (Fig. 1 and fig. S2). In HS3, a Tyr side chain forms a hydrogen bond to Asp^{19} on HA2 and van der Waals interactions with the A helix on HA2. The Tyr in HS3 resembles the conformation of a Tyr residue observed on the antibody in the structure of the HA and CR6261 Fab complex (figs. S1 and S2); the HS1 and HS2 interactions are not found in the antibody structures (*9*, *10*, *17*) (fig. S1).

In the second step, we searched a set of 865 protein structures selected for ease of experimental manipulation (*18*) (table S1) for scaffolds capable of supporting the disembodied hot spot residues and that are shape complementary to the stem region. Each scaffold protein was docked against the stem region using the feature-matching algorithm PatchDock (*19*), which identified hun-

---

[1]Department of Biochemistry, University of Washington, Seattle, WA 98195, USA. [2]Department of Molecular Biology and the Skaggs Institute for Chemical Biology, The Scripps Research Institute, 10550 North Torrey Pines Road, La Jolla, CA 92037, USA. [3]Howard Hughes Medical Institute, University of Washington, Seattle, WA 98195, USA.

*These authors contributed equally to this manuscript.
†Present address: Genentech, 1 DNA Way, South San Francisco, CA 94080, USA.
‡To whom correspondence should be addressed. E-mail: dabaker@uw.edu

dreds of compatible binding modes for each scaffold (260,000 in total). These coarse-grained binding modes were then refined using RosettaDock (*20*) with a potential scoring function that favored configurations that maximized the compatibility of the scaffold protein backbone with as many hot spot residues as possible (*14*). Next, residues from the hot spot residue libraries were incorporated onto the scaffold. First, for each Phe conformation in HS1, scaffold residues with backbone atoms within 4 Å of the hot spot residue were identified. For each of these candidate positions, the scaffold protein was placed to coincide with the backbone of the hot spot, the residue was modeled explicitly, and the rigid-body orientation was optimized. If no steric clashes were observed and the Phe was in contact with Trp^{21} and Thr^{41} of HA2 (Fig. 2B), the placement of the first hot spot residue was deemed successful; otherwise, another HS1 Phe conformation was selected and the process was repeated. For each success with HS1, an attempt was made to realize the HS2 interactions by incorporating nonpolar residues at appropriate positions in the scaffold protein, and the remainder of the scaffold protein surface was then redesigned using RosettaDesign (*21*).

Designing proteins also containing HS3 interactions was more challenging because of the large number of combinations of residue placements to be considered. To generate designs containing all three hot spot regions, we started by superimposing the scaffold protein on the backbone of the Tyr residue in HS3 (as for the Phe HS1 residue above). We then searched for two positions on the scaffold protein that were nearest to residues in HS1 and HS2 and were best aligned to them (*14*). These positions were then simultaneously designed to Phe in the case of HS1 and to nonpolar residues in the case of HS2. RosettaDesign (*21*) was then used to redesign the remainder of the interface on the scaffold protein, with sequence changes allowed within a distance of 10 Å of the HA.

Experimental and Structural Characterization

A total of 51 designs with the two–hot spot–residue concept and 37 with the three-residue concept were selected for testing (table S2 in SOM text and supplemental coordinate files of all models). The designs are derived from 79 different protein scaffolds and differ from the scaffold by on average 11 mutations. Genes encoding the designs were synthesized, cloned into a yeast-display vector, and transformed into yeast strain EBY100 (*22*). Upon induction, the designed protein is displayed on the cell surface as a fusion between the yeast Aga2p protein and a C-terminal c-Myc tag. Cells expressing designs were incubated with 1 μM of biotinylated SC1918/H1 [A/South Carolina/1/1918 (H1N1)] HA ectodomain, washed, and dual-labeled with phycoerythrin-conjugated streptavidin and fluorescein-conjugated antibody against c-Myc. Display of the designed protein on the yeast surface and binding to HA were simultaneously measured by flow cytometry.

Of the 73 designs that displayed on the yeast surface, 2 showed reproducible binding activity toward the HA stem region (*23*) (table S2) (for models, see Fig. 2, C to F). One design, HA binder 36 (HB36) used the two-residue hot spot and bound to the HA with an apparent dissociation constant (K_d) of 200 nM (*24*) (Fig. 2G and fig. S4). The starting scaffold, structural genomics target APC36109, a protein of unknown function from *Bacillus stearothermophilus* [Protein Data Bank (PDB) entry 1U84], did not bind HA (fig. S4), which indicated that binding is mediated by

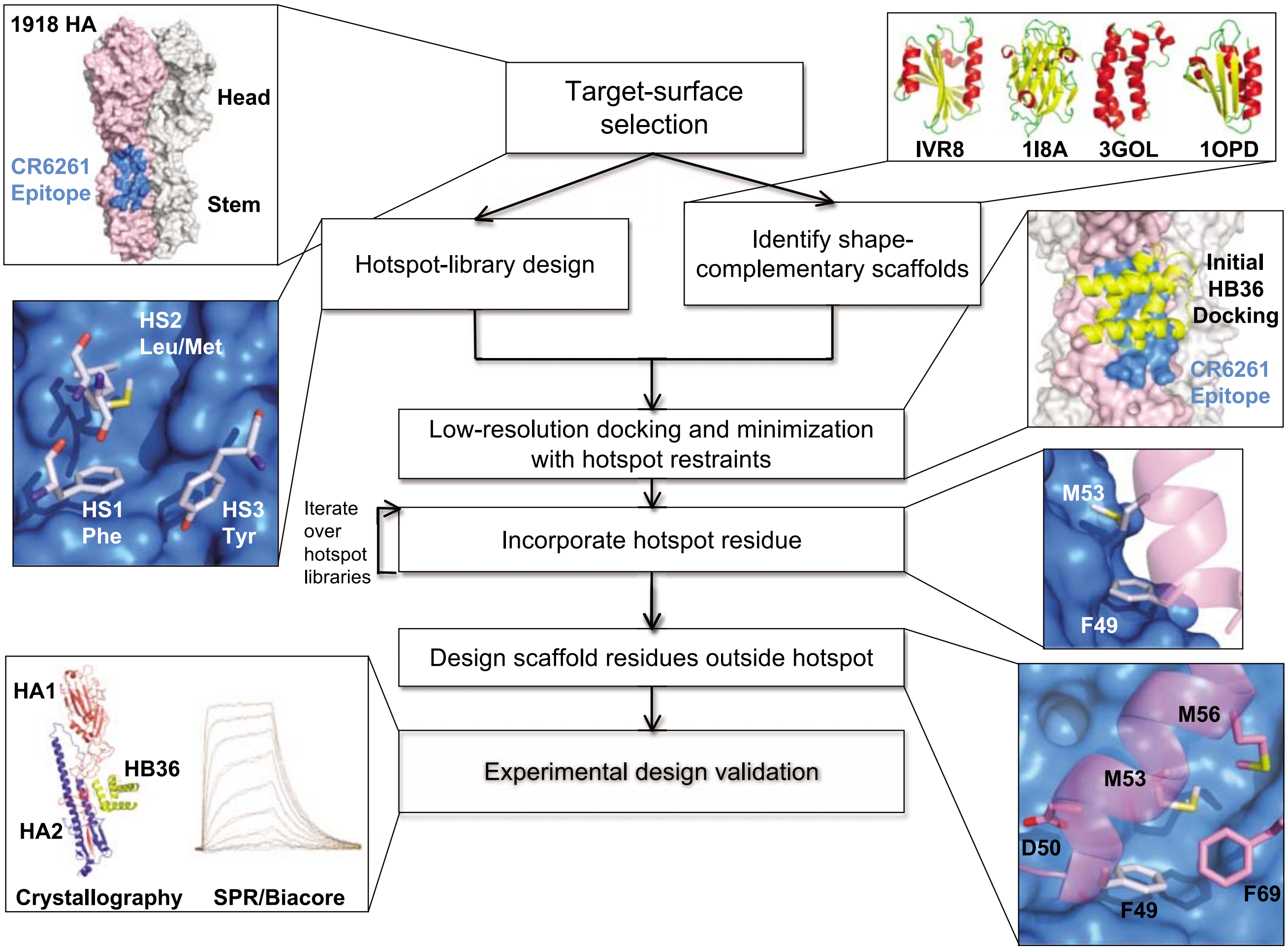
1918 HA
Head
CR6261 Epitope
Stem
Target-surface selection
IVR8
1I8A
3GOL
1OPD
Hotspot-library design
Identify shape-complementary scaffolds
HS2 Leu/Met
HS1 Phe
HS3 Tyr
Initial HB36 Docking
CR6261 Epitope
Low-resolution docking and minimization with hotspot restraints
Iterate over hotspot libraries
Incorporate hotspot residue
M53
F49
Design scaffold residues outside hotspot
Experimental design validation
HA1
HB36
HA2
Crystallography
SPR/Biacore
M56
M53
D50
F49
F69

Fig. 1. Flow chart illustrating the key steps in the design of novel binding proteins. The thumbnails illustrate each step in the creation of binders that target the stem of the 1918 HA. Abbreviations (*29*).

the designed surface on HB36. A second design, HB80, used the three-residue hot spot and bound HA only weakly (Fig. 2H). The scaffold from which this design was derived, the MYB domain of the RAD transcription factor from *Antirrhinum majus* (PDB code: 2CJJ) (*25*), again did not bind the HA (fig. S5).

In the computational models of the two designs (Fig. 2, C to F), the hot spot residues are buttressed by a concentric arrangement of hydrophobic residues with an outer ring of polar and charged residues as is often observed in native protein-protein interfaces. Both designs present a row of hydrophobic residues on a helix that fits into the HA hydrophobic groove. The complexes each bury ~1550 Å^2 surface area (total), close to the mean value for dissociable protein interactions (*12*) and slightly larger than the total surface area buried by each of the two neutralizing antibodies (*9*, *10*) (fig. S1). The helical binding modes in these designs are very different from the loop-based binding observed in the antibody-bound structures.

Affinity Maturation

The computational design protocol is far from perfect; the energy function that guides design contains numerous approximations (*26*), and conformational sampling is incomplete. We used affinity maturation to identify shortcomings in the design protocol. Libraries of HB36 and HB80 variants were generated by single site–saturation mutagenesis at the interface, or by error-prone polymerase chain reaction (epPCR), and subjected to two rounds of selection for binding to HA using yeast surface display (*22*).

For both designed binders, the selections converged on a small number of substitutions that increase affinity and provide insight into how to improve the underlying energy function. Among the key contributions to the energetics of macromolecular interactions are short-range repulsive interactions due to atomic overlaps, electrostatic interactions between charged and polar atoms, and the elimination of favorable interactions with solvent (desolvation). The affinity-increasing substitutions point to how each of these contributions can be better modeled in the initial design calculations.

Repulsive interactions. For HB36, replacement of Ala^{60} with the isosteres Thr and Val increased the apparent binding affinity 25-fold (apparent K_d values for all design variants are listed in Table 1). These substitutions fill a void between the designed protein and the HA surface, but were not included in the original design because they were disfavored by steric clashes within HB36 (Fig. 3A). Backbone minimization, however, readily relieved these clashes and resulted in higher predicted affinity for the substitutions. More direct incorporation of backbone minimization in the design algorithm should allow identification of such favorable interactions from the start. For HB80, a M26T mutation significantly increased binding compared with the starting design; modeling suggested that Met^{26} disfavored the conformation of the Tyr hot spot residue (Fig. 3B). The design process should ensure that residues, which make favorable interactions across the interface, also make favorable interactions in the unbound state of the designed protein.

Electrostatics. In HB36, the substitution with Lys at position 64 places a complementary charge adjacent to an acidic pocket on HA near the conserved stem region (Fig. 3C); in HB80, an N36K substitution positions a positive charge 6.5 Å from the negative Asp^{19} on HA2 (Fig. 3D). These substitutions enhance electrostatic complementarity in the complex. The lysines were not selected in the design calculations because the magnitude of surface electrostatic interactions between atoms outside of hydrogen-bonding range are largely reduced; improvement of the electrostatic model would evidently allow design of higher-affinity binders from the start.

Desolvation. In HB36, eight different substitutions at Asp^{47} increased apparent affinity by more than an order of magnitude compared with the original design (table S3); the highest-affinity substitution was D47S, which increased binding

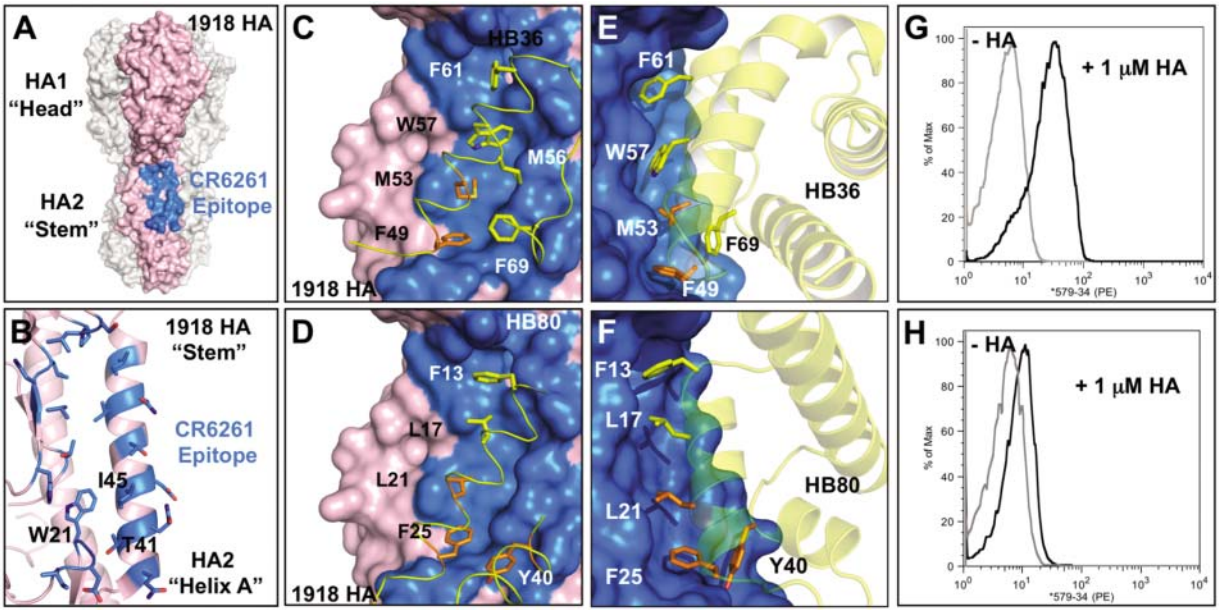

Fig. 2. The HB36 and HB80 designs target the stem of the 1918 HA. (**A**) Surface representation of the trimeric HA structure (PDB 3R2X) from the 1918 pandemic virus, with one of the three protomers highlighted in pink. Broadly neutralizing antibody CR6261 binds a highly conserved epitope in the stem region (blue patch on surface), close to the viral membrane (bottom). (**B**) Enlarged view of the CR6261 epitope [blue region from (A)], with CR6261 contact residues depicted as sticks. This target site on HA contains a groove lined by multiple hydrophobic residues. Loops on either side of this hydrophobic groove (above and below) constrain access to this region. Key residues on HA2 are noted. (**C** and **D**) Front view of the designed interaction between HB36 (C) and HB80 (D) and the target site on HA. HA is rotated ~45° relative to (A). Contact segments of HB36 and HB80 are colored yellow, and residues are depicted as sticks, with hot spot residues highlighted in orange (F49 and M53 for HB36 and L21, F25, and Y40 for HB80). Polar atoms of side chains are shown in red (oxygen) and blue (nitrogen). For clarity, the noncontacting regions from the designs have been omitted. (**E** and **F**) Side view of the designed interactions of HB36 (E) and HB80 (F) with 1918/H1 HA. (**G** and **H**) Initial binding data for HB36 (G) and HB80 (H) designs (before affinity maturation). When incubated with 1 μM 1918 HA, yeast displaying the two designed proteins show an increase in fluorescent phycoerythrin signal (*x* axis) compared with the absence of 1918 HA. Coordinate files of models of 1918 HA in complex with HB36 and HB80 are available as SOM.

affinity about 40-fold. The design calculations underestimated the energetic cost of desolvating Asp^{47} by the aliphatic Ile^{18} on HA2 (Fig. 3E); the substitutions remedy this error by replacing the Asp with residues that are less costly to desolvate upon binding. In HB80, a D12G substitution relieves the desolvation by the neighboring Ile^{56} on HA2 (Fig. 3F). With improvements in the solvation model, the deleterious Asp residues would not be present in starting designs.

The favorable substitutions were combined, and the proteins were expressed with a His tag in *Escherichia coli* and purified by nickel-affinity and size-exclusion chromatography. The variant HB36.3, incorporating the D47S and A60V substitutions, bound to SC1918/H1 HA as confirmed by surface plasmon resonance (SPR) (fig. S6), enzyme-linked immunosorbent assay (ELISA), and coelution on a size-exclusion column (fig. S7). The HB36.4 variant, which incorporates D47S, A60V, and N64K, bound to SC1918/H1 HA with a dissociation constant measured by SPR of 22 nM and an off-rate of 7×10^{-3} s^{-1} (table S4). Coincubation with an excess of CR6261 Fab abolished binding to the HA (Fig. 3G), consistent with HB36.4 binding in close proximity to the same stem epitope on the HA. For the HB80 design, the combination of the affinity-increasing mutations reduced surface expression on yeast, indicative of poor stability. Therefore, we excised a C-terminal stretch (Δ54–95) greatly boosting surface expression of the design with no significant loss of binding affinity (fig. S9). HB80.3, which incorporates the truncation as well as the D12G, A24S, M26T, and N36K substitutions, has a K_d = 38 nM with off-rate of 4×10^{-2} s^{-1} by SPR. As with HB36.4, coincubating HA with the CR6261 Fab completely abolished binding to HB80.3 (Fig. 3H), consistent with the designed binding mode.

Alanine substitutions at core positions on each affinity-matured design partially or completely knocked out HA binding (table S5 and fig. S10), which supported the computational models of the designed interfaces (*27*). No mutations were uncovered during selection for higher affinity that were inconsistent with the designed binding modes.

Table 1. Summary of dissociation constants between SC1918/H1 HA and selected design variants. Apparent K_d was determined using yeast surface display titrations. Numbers in parentheses indicate K_d determined by SPR. NB, no binding.

Design	K_d (nM)
1U84 (HB36 scaffold)	NB (NB)
HB36	200 (>2000)
HB36 D47S	5
HA36 A60V	8
HB36.3 (HB36 D47S, A60V)	4 (29)
HB36.4 (HB36 D47S, A60V, N64K)	4 (22)
2CJJ (HB80 scaffold)	NB
HB80	>5000
HB80 M26T	100
HB80 N36K	300
HB80 M26T N36K	7.5
HB80 Δ54-95, M26T, N36K	5
HB80.3 (HB80 Δ54-95, D12Gly, A24S, M26T, N36K)	3 (38)

Crystal Structure of the HB36.3-SC1918 HA Complex

The crystal structure of HB36.3 in complex with the SC1918 HA ectodomain was determined to 3.1 Å resolution. After molecular replacement using only the 1918/H1 HA structure as the search model (~86% of the protein mass in the crystal asymmetric unit), clear electron density was observed for HB36.3 near the target surface in the HA stem region into which HB36.3 could be unambiguously placed. The orientation was essentially identical to the designed binding mode, with the modified surface of the main recognition helix packed in the hydrophobic groove on HA (Fig. 4, A and B). To obtain unbiased density for the designed side chains, the native structure from which HB36.3 was

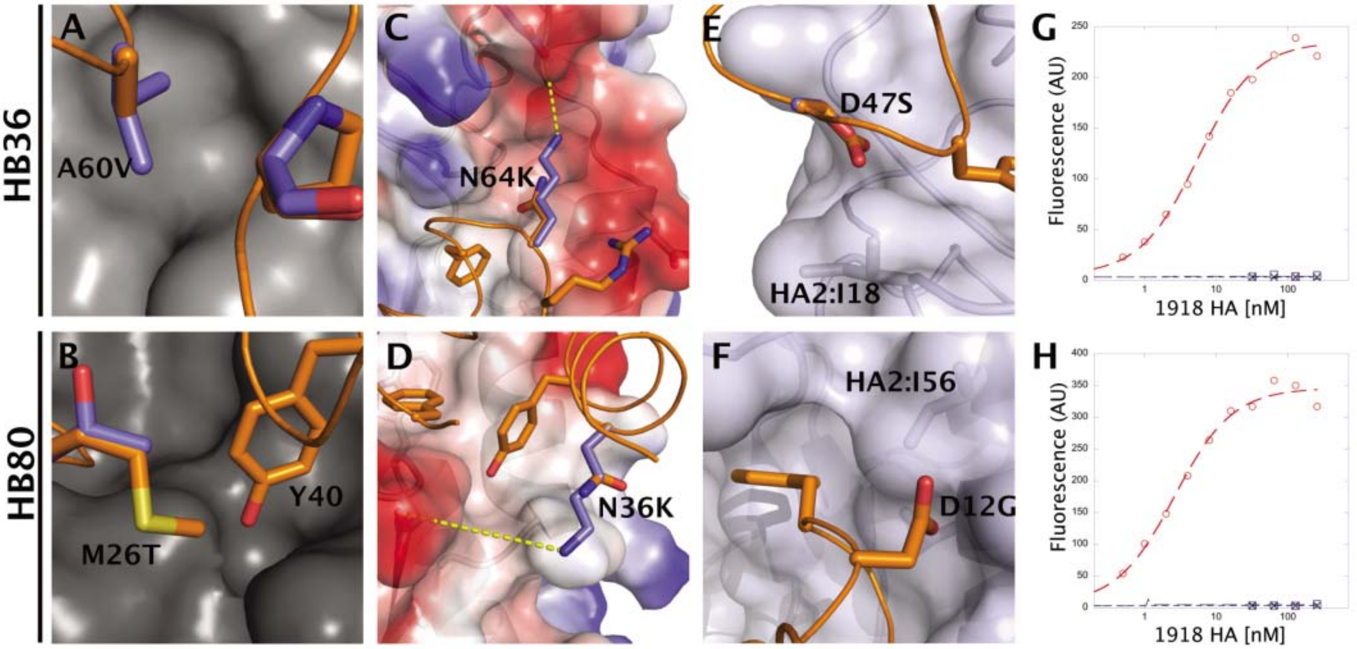

Fig. 3. Affinity maturation. Substitutions that increase the affinity of the original designs reflect deficiencies in modeling the (**A** and **B**) repulsive interactions HB36 A60V (A), HB80 M26T (B); (**C** and **D**) electrostatics HB36 N64K (C), HB80 N36K (D); and (**E** and **F**) solvation HB36 D47S (E), HB80 D12G (F). Binding titrations of HB36.4 (**G**) and HB80.3 (**H**) to SC1918/H1 HA as measured by yeast surface display. Red circles represent the affinity-matured design; blue squares, the scaffold protein from which the design is derived; and black crosses, the design in the presence of 750 nM inhibitory CR6261 Fab.

derived (PDB entry: 1U86) was manually fit into the electron-density maps, and designed side chains were pruned back to their β carbon. After crystallographic refinement, electron density became apparent for the side chains of most of the contact residues on HB36.3, which allowed the predominant rotamers to be assigned for Phe^{49}, Trp^{57}, Phe^{61}, and Phe^{69}. This unbiased density clearly shows that these four hydrophobic side chains are all positioned as in the designed model (Fig. 4C). The Met^{53} side chain is consistent with the design model, although other rotamers could also be fit to the map. For Met^{56}, only very weak side-chain density was observed. Overall, the crystal structure is in excellent agreement with the designed interface, with no significant deviations at any of the contact positions.

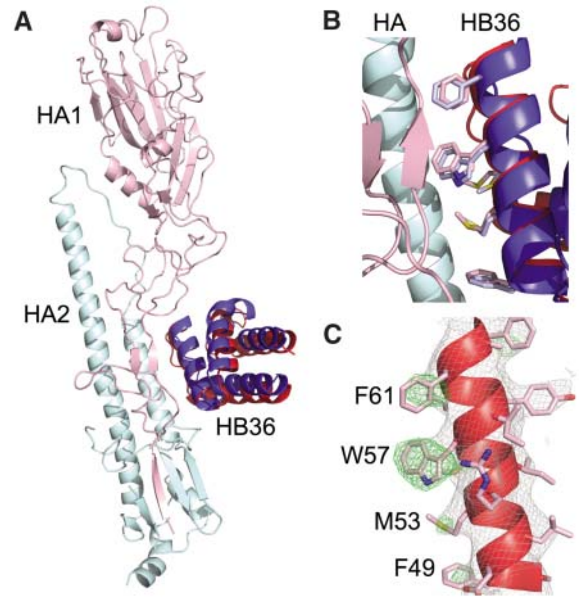

Fig. 4. Crystal structure of HB36.3-SC1918/H1 complex shows the precision of the computational design. (**A**) Superposition of the crystal structure of HB36.3-SC1918/H1 complex (HB36.3 in red with SC1918 HA1 subunit in pink and HA2 subunit in cyan) and the computational design (blue) reveals good agreement in the position of the main recognition helix, with a slight rotation of the rest of the protein domain. Superposition was performed using the HA2 subunits. For clarity, only the HA from the crystal structure is depicted here (the HA used for superposition of the design, which is essentially identical to the crystal structure, was omitted). (**B**) Close up of the SC1918 HA-HB36.3 interface, highlighting the close agreement between the design and the crystal structure. The main recognition helix is oriented as in (A), with the HB36.3 crystal structure in red (pink side chains), the design in blue (light blue side chains), and HA in cyan and pink at left. (**C**) Unbiased $2F_{obs} - F_{calc}$ (gray mesh, contoured at 1σ) and $F_{obs} - F_{calc}$ (green mesh, contoured at 3σ) electron-density maps for the main recognition helix of HB36.3. The helix is oriented as in (B), with key HA-contacting residues labeled (residues on the right of the helix interact with the core of HB36). Additional density was observed for most of the large side chains at the interface with HA, including F49, M53, W57, F61, and F69 (not visible in this view). Although side chains are shown here to illustrate their agreement with the experimental electron density, maps were calculated after initial refinement of an HA-HB36.3 model with the interface side chains F49, M53, M56, W57, F61, and F69 truncated to alanine.

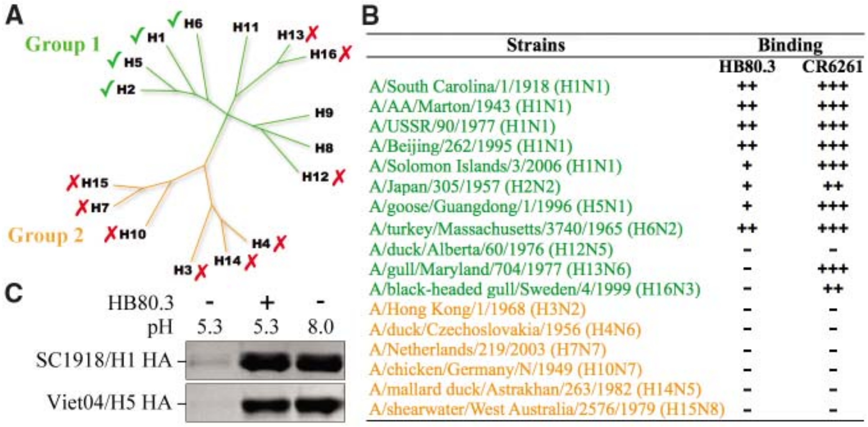

Strains	Binding	
	HB80.3	CR6261
A/South Carolina/1/1918 (H1N1)	++	+++
A/AA/Marton/1943 (H1N1)	++	+++
A/USSR/90/1977 (H1N1)	++	+++
A/Beijing/262/1995 (H1N1)	++	+++
A/Solomon Islands/3/2006 (H1N1)	+	+++
A/Japan/305/1957 (H2N2)	+	++
A/goose/Guangdong/1/1996 (H5N1)	+	+++
A/turkey/Massachusetts/3740/1965 (H6N2)	++	+++
A/duck/Alberta/60/1976 (H12N5)	-	-
A/gull/Maryland/704/1977 (H13N6)	-	+++
A/black-headed gull/Sweden/4/1999 (H16N3)	-	++
A/Hong Kong/1/1968 (H3N2)	-	-
A/duck/Czechoslovakia/1956 (H4N6)	-	-
A/Netherlands/219/2003 (H7N7)	-	-
A/chicken/Germany/N/1949 (H10N7)	-	-
A/mallard duck/Astrakhan/263/1982 (H14N5)	-	-
A/shearwater/West Australia/2576/1979 (H15N8)	-	-

Fig. 5. HB80.3 binds and inhibits multiple HA subtypes. (**A**) Phylogenetic tree depicting the relation between the 16 influenza A HA subtypes. These subtypes can be divided into two main lineages, groups 1 and 2. CR6261 has broad activity against group 1 viruses. HB80.3 has a similar cross-reactivity profile and binds multiple group 1 subtypes, including H1 and H5. (**B**) Binding data for HB80.3 and CR6261 Fab against a panel of HAs. +, ++, and +++ indicate relative degree of binding (dissociation constant approximately 10^{-7}, 10^{-8}, and 10^{-9} M, respectively), whereas a minus sign (–) indicates no detectable binding at the highest concentration tested (100 nM). (**C**) HB80.3 inhibits the pH-induced conformational changes that drive membrane fusion. Exposure to low pH converts 1918 H1 HA (top) and the Viet04 H5 HA to a protease-susceptible state (lane 1), whereas HAs maintained at neutral pH are highly resistant to trypsin (lane 3). Preincubation of HB80.3 with H1 and H5 prevents pH-induced conformational changes and retains the HAs in the protease-resistant, prefusion state (lane 2).

Given the quite low (2 out of the 73 surface-displayed proteins) design success rate and starting affinities, the atomic-level agreement between the designed and experimentally determined HB36.3–SC1918 HA complex is very encouraging and suggests that, despite their shortcomings, the current energy function and design methodology capture essential features of protein-protein interactions.

Cross-Reactivity and Inhibitory Activity

The surface contacted by HB36.3 is accessible and highly conserved in the HAs of most group 1 influenza viruses, which suggests that it may be capable of binding not only other H1 HAs, but also other HA subtypes. Indeed, binding of HB36.3 to A/South Carolina/1/1918 (H1N1) and A/WSN/1933 (H1N1) is readily detectable in solution by gel filtration (fig. S7), as is high-affinity binding of HB36.4 to A/Vietnam/1203/2004 H5 subtype by yeast display (fig. S11).

Although a crystal structure of HB80 in complex with HA has not been obtained, the mutational data and the antibody-competition results suggest that HB80 also binds to the designed target surface and overlaps with HB36 and CR6261. Consequently, HB80.3 is also expected to be highly cross-reactive and, indeed, binds with high affinity to A/Vietnam/1203/2004 H5 HA (fig. S11) and to H1, H2, H5, and H6 subtypes in biolayer interferometry experiments (Fig. 5, A and B). Overall, HB80 binds most of the group 1 HAs tested but does not have detectable binding to group 2 HAs, mirroring the binding profile of CR6261.

Antibody CR6261 inhibits influenza virus replication by blocking the pH-induced refolding of HA, which drives fusion of the viral envelope with the endosomal membrane of the host cell. Given extensive overlap between the HB80.3 and CR6261 binding sites and its high affinity for SC1918 HA, it seemed plausible that HB80.3 would also block this conformational change. Indeed, HB80.3 inhibits the pH-induced conformational changes in both H1 and H5 HAs (Fig. 5C and fig. S12) (*10*), which suggests that this design may have virus-neutralizing activity against multiple influenza subtypes (*28*). Further work will be needed to explore the potential utility of HB80.3 in a therapeutic or diagnostic setting, but these results suggest that de novo computational design of antiviral proteins is feasible.

References and Notes

1. H. Ledford, *Nature* **455**, 437 (2008).
2. R. A. Lerner, *Angew. Chem. Int. Ed. Engl.* **45**, 8106 (2006).

3. T. Kortemme *et al.*, *Nat. Struct. Mol. Biol.* **11**, 371 (2004).
4. R. K. Jha *et al.*, *J. Mol. Biol.* **400**, 257 (2010).
5. P. S. Huang, J. J. Love, S. L. Mayo, *Protein Sci.* **16**, 2770 (2007).
6. J. Karanicolas *et al.*, *Mol. Cell* **42**, 250 (2011).
7. S. Liu *et al.*, *Proc. Natl. Acad. Sci. U.S.A.* **104**, 5330 (2007).
8. Writing Committee of the WHO Consultation on Clinical Aspects of Pandemic (H1N1) 2009 Influenza, *N. Engl. J. Med.* **362**, 1708 (2010).
9. J. Sui *et al.*, *Nat. Struct. Mol. Biol.* **16**, 265 (2009).
10. D. C. Ekiert *et al.*, *Science* **324**, 246 (2009).
11. Group 1 includes 10 of the 16 HA subtypes: H1, H2, H5, H6, H8, H9, H11, H12, H13, and H16. Group 2 includes the remaining six subtypes: H3, H4, H7, H10, H14, and H15.
12. L. Lo Conte, C. Chothia, J. Janin, *J. Mol. Biol.* **285**, 2177 (1999).
13. T. Clackson, J. A. Wells, *Science* **267**, 383 (1995).
14. Materials and methods are available as supporting material on *Science* Online.
15. M. G. Rossmann, *J. Biol. Chem.* **264**, 14587 (1989).
16. J. Chen, J. J. Skehel, D. C. Wiley, *Proc. Natl. Acad. Sci. U.S.A.* **96**, 8967 (1999).
17. The other hot spot residues (HS1 and HS2) differed from the side chains observed in the crystal structures in their conformation or identity. Each hot spot residue was further diversified by constructing all conformations, the terminal atoms of which coincided with those modeled above. For instance, for HS3, these consisted of all Tyr conformations that matched the position of the aromatic ring and hydrogen bond. This diversification step produced a "fan" of backbone positions for each residue in the hot spot libraries.
18. Proteins in the scaffold set contained no disulfides, were expressed in *E. coli*, and were predicted to form monomers (*14*).
19. D. Schneidman-Duhovny, Y. Inbar, R. Nussinov, H. J. Wolfson, *Nucleic Acids Res.* **33** (Web Server issue), W363 (2005).
20. J. J. Gray *et al.*, *J. Mol. Biol.* **331**, 281 (2003).
21. B. Kuhlman *et al.*, *Science* **302**, 1364 (2003).
22. G. Chao *et al.*, *Nat. Protoc.* **1**, 755 (2006).
23. A third design HB35 bound HA at apparent low-micromolar affinity; however, binding was only partially abolished upon coincubation of HA with the CR6261 Fab, which indicated, at most, partial contact with the target surface on the stem region of HA, and so this design was eliminated from further consideration (fig. S7). A handful of other designs bound HA, albeit weakly and with incomplete reproducibility (*14*).
24. We recorded dissociation constants using two main methods: by titration of HA against yeast surface-displayed designs and by fitting both kinetic and equilibrium measurements using surface plasmon resonance. As there is a discrepancy in determining K_d values between the methods, measurements derived from yeast surface-display titrations are listed as apparent K_d and should be viewed qualitatively (*14*).
25. C. E. Stevenson *et al.*, *Proteins* **65**, 1041 (2006).
26. R. Das, D. Baker, *Annu. Rev. Biochem.* **77**, 363 (2008).
27. The alanine-scan mutations were as follows: for HB36.3, Phe^{49}, Met^{53}, and Trp^{57}; for HB80.1 Phe^{13}, Phe^{25}, and Tyr^{40} (table S4 and SOM text).
28. HB36.3 was not able to block the pH-induced conformational changes in the H1 and H5 HAs under identical assay conditions, even though HB36.3 and HB80.3 have very similar dissociation constants and kinetic off-rates at pH 7.5 (fig. S12 and SOM text).
29. Single-letter abbreviations for the amino acid residues are as follows: A, Ala; C, Cys; D, Asp; E, Glu; F, Phe; G, Gly; H, His; I, Ile; K, Lys; L, Leu; M, Met; N, Asn; P, Pro; Q, Gln; R, Arg; S, Ser; T, Thr; V, Val; W, Trp; and Y, Tyr.

Acknowledgments. Computational designs were generated on resources generously provided by participants of Rosetta @ Home and the Argonne National Leadership Computing Facility. We thank J. L. Gallaher for protein preparation. S.J.F. was supported by a long-term fellowship from the Human Frontier Science Program, J.E.C. was supported by the Jane Coffin Childs Memorial Fund, and E.M.S. by a career development award from the National Institute of Allergy and Infectious Diseases, NIH, AI057141. Research in the Baker laboratory was supported by grants from the Defense Advanced Research Projects Agency, the NIH yeast resource center, the Defense Threat Reduction Agency, and the Howard Hughes Medical Institute and in the Wilson laboratory by NIH AI058113, predoctoral fellowships from the Achievement Rewards for College Scientists Foundation and the NIH Molecular Evolution Training Program GM080209 (D.C.E.), and the Skaggs Institute for Chemical Biology. X-ray diffraction data sets were collected at the Stanford Synchrotron Radiation Lightsource beamline 9-2 and at the Advanced Photon Source (APS) beamline 23ID-B (GM/CA-CAT). The GM/CA CAT 23-ID-B beamline has been funded in whole or in part with federal funds from National Cancer Institute (Y1-CO-1020) and the National Institute of General Medical Science, NIH (Y1-GM-1104). Use of the APS was supported by the U.S. Department of Energy, Basic Energy Sciences, Office of Science, under contract no. DE-AC02-06CH11357. Coordinates and structure factors were deposited in the Protein Data Bank as entry 3R2X.

Supporting Online Material
www.sciencemag.org/cgi/content/full/332/6031/816/DC1
Materials and Methods
SOM Text
Figs. S1 to S12
Tables S1 to S7
References

7 January 2011; accepted 8 April 2011
10.1126/science.1202617

REPORTS

Interplay of Rotational, Relaxational, and Shear Dynamics in Solid ^{4}He

E. J. Pratt,[1,2]* B. Hunt,[1,3]* V. Gadagkar,[1] M. Yamashita,[4] M. J. Graf,[5] A. V. Balatsky,[5] J. C. Davis[1,6,7]†

Using a high-sensitivity torsional oscillator (TO) technique, we mapped the rotational and relaxational dynamics of solid helium-4 (^{4}He) throughout the parameter range of the proposed supersolidity. We found evidence that the same microscopic excitations controlling the torsional oscillator motions are generated independently by thermal and mechanical stimulation. Moreover, a measure for the relaxation times of these excitations diverges smoothly without any indication for a critical temperature or critical velocity of a supersolid transition. Finally, we demonstrated that the combined temperature-velocity dependence of the TO response is indistinguishable from the combined temperature-strain dependence of the solid's shear modulus. This implies that the rotational responses of solid ^{4}He attributed to supersolidity are associated with generation of the same microscopic excitations as those produced by direct shear strain.

Solid ^{4}He may become a supersolid (*1*) when its temperature T and mass-flow velocity V fall below their critical (*2*) values T_c and V_c. Indeed, torsional oscillator (TO) studies (*3*, *4*) reveal that the resonant angular frequency of rotation ω increases rapidly below both $T \sim 250$ mK and rim velocity $V \sim 10^{-4}$ ms^{-1}, as if superfluid inertia decouples at a critical temperature and velocity. These ω increases (*3*–*10*) are greatly diminished by blocking the TO annulus (*4*, *11*), as if superfluid inertia is thereby reconnected. Signatures in the heat capacity ascribed to supersolidity also occur in this same temperature range (*12*). However, direct mass-flow studies detect maximum currents that are far smaller than those implied by the TO experiments (*13*–*15*). Moreover, the temperature dependence of the resonance frequency $f(T) = \omega(T)/2\pi$ of TOs containing solid ^{4}He (*3*–*11*) resembles closely that of its shear modulus $\mu(T)$ (*16*). Coincident with the maximum rates of increase of $f(T)$ and $\mu(T)$ are maxima in TO dissipation (*4*–*6*, *8*, *9*) and shear dissipation (*16*, *17*), respectively. Such effects should not exist during a bulk Bose-Einstein condensation transition, although they do occur in the Berezinskii-Kosterlitz-Thouless (BKT) transition of a superfluid film (*18*) [see Supporting Online Material (SOM) section I (*19*)]. Finally, the increases in both f and μ are quickly extinguished by increasing TO maximum rim velocity V (*3*–*8*, *10*) or shear strain ε (*16*, *20*), respectively.

Several theoretical models have been proposed to explain the unexpectedly complex rotational dynamics of solid ^{4}He. The first is a simple supersolid (*1*) in which Bose-Einstein condensation of vacancies produces an inter-

---

[1] Laboratory for Atomic and Solid State Physics, Department of Physics, Cornell University, Ithaca, NY 14853, USA. [2] Kavli Institute for Theoretical Physics, University of California, Santa Barbara, CA 93016, USA. [3] Department of Physics, Massachusetts Institute of Technology, Cambridge, MA 02139, USA. [4] Department of Physics, Kyoto University, Kyoto 606-8502, Japan. [5] Theoretical Division and Center for Integrated Nanotechnologies, Los Alamos National Laboratory, Los Alamos, NM 87545, USA. [6] Condensed Matter Physics and Materials Science Department, Brookhaven National Laboratory, Upton, NY 11973, USA. [7] School of Physics and Astronomy, University of St. Andrews, St. Andrews, Fife KY16 9SS, UK.

*These authors contributed equally to this work.
†To whom correspondence should be addressed. E-mail: jcdavis@ccmr.cornell.edu